European Journal of Medicinal Chemistry 193 (2020) 112234

Contents lists available at ScienceDirect

European Journal of Medicinal Chemistry

journal homepage: http://www.elsevier.com/locate/ejmech

Research paper

Synthesis and biological evaluation of gold(III) Schiff base complexes for the treatment of hepatocellular carcinoma through attenuating TrxR activity

Mianli Bian [a], Xin Wang [a], Ying Sun [a], Wukun Liu [a, b, c, *]

[a] School of Pharmacy, Nanjing University of Chinese Medicine, Nanjing, 210023, PR China
[b] State Key Laboratory of Natural Medicines, China Pharmaceutical University, Nanjing, 210009, PR China
[c] State Key Laboratory of Coordination Chemistry, Nanjing University, Nanjing, 210023, PR China

ARTICLE INFO

Article history:
Received 29 January 2020
Received in revised form
4 March 2020
Accepted 11 March 2020
Available online 14 March 2020

Keywords:
Gold(III) Schiff base complexes
Thioredoxin reductase
Reactive oxygen species
Endoplasmic reticulum stress
Hepatocellular carcinoma

ABSTRACT

Hepatocellular carcinoma (HCC) is one of the most common cancers and a leading cause of death worldwide. Increased thioredoxin reductase (TrxR) levels were recently identified as possible prognostic markers for HCC. Here, four gold(III) complexes **1b-4b** bearing Schiff base ligands were synthesized, characterized, and screened for antitumor activity against HCC. All complexes triggered significant antiproliferative effects against HCC cells, especially the most active complex **1b** induced HepG2 cells apoptosis by activating the endoplasmic reticulum stress (ERS). **1b** could clearly inhibit the TrxR activity to elevate reactive oxygen species (ROS), mediate ERS and lead to mitochondrial dysfunction. Notably, treatment of **1b** improved the CCl_4-induced liver damage *in vivo* by down-regulation of TrxR expression and inflammation level.

1. Introduction

Hepatocellular carcinoma (HCC) is the most common and high incidence disease in all types of cancer [1]. It is associated with underlying chronic liver disease, accounting for 85–90% of primary liver cancer [2,3]. Although significant progress has been achieved in traditional treatment for HCC, it remains the most lethal malignancies globally due to limited restricted therapeutics, high recurrence rate and poor prognosis [4]. Thus, identifying the safest and most effective treatments for HCC have never been more urgent.

Thioredoxin reductase (TrxR), as a major cellular protein transfers the electron for reactive oxygen species (ROS) scavenging, has been suggested as a prognostic marker for human HCC patients [5]. Many studies have shown that TrxR was involved in multifarious physiological and pathological processes, including apoptosis, chronic inflammation and cancer [6]. Increasing evidences show that TrxR is an irreplaceable modulator during the development of tumor [7,8]. Thus, increased expression of TrxR in clinical samples positively correlated with advanced clinical staging and poorer patient survival. TrxR level has also been recognized as a promising survival indicator in patients with HCC [9,10]. These results strongly suggest that inhibition of TrxR is a very significant clinical goal. TrxR is therefore a novel potential target for the treatment of HCC.

In this regard, gold complexes and particularly auranofin (an anti-rheumatoid arthritis drug), which are the most efficacious TrxR inhibitors, have been essayed as biological active products in cancers including HCC [11]. Auranofin has high affinity for selenocysteine residues within the redox-active domain of TrxR, and it forms an irreversible and stable adduct, blocking the activity of TrxR [5,12–16]. In addition, auranofin is nowadays actively being repurposed in pilot trials and clinical studies for anticancer therapy against chronic lymphocytic leukaemia (NCT01419691) and ovarian cancer (NCT01747798) among others [11,17].

However, most of gold complexes including auranofin are insufficient physiological stability. They are readily metabolized by thiol-containing biomolecules [18–21]. Besides, the coordinated ligands of these gold complexes are mostly lost before target enzymes such as TrxR are reached [22]. Therefore, there is a growing interest in the development of more stable gold-based agents and

* Corresponding author. School of Pharmacy, Nanjing University of Chinese Medicine, Nanjing, 210023, PR China.
E-mail addresses: liuwukun0000@hotmail.com, liuwukun0000@njucm.edu.cn (W. Liu).

https://doi.org/10.1016/j.ejmech.2020.112234
0223-5234/

Abbreviations used

CD	circular dichroism
CDKs	cyclin dependent protein kinases
CHOP	C/EBP homologous protein
CT-DNA	calf thymus DNA
ER	endoplasmic reticulum
ERS	endoplasmic reticulum stress
GRP78	glucose-regulated protein 78
GSH	glutathione
HCC	hepatocellular carcinoma
LDH	lactate dehydrogenase
MMP	mitochondrial membrane potential
NAC	*N*-acetylcysteine
ROS	reactive oxygen species
Sal	salubrinal
TrxR	thioredoxin reductase

the fine tuning of their ligands due to the strong metabolization of gold metallodrugs [18,23–27].

Here, in order to find an improved, more stable, gold-based TrxR inhibitor, we developed a series of gold(III) complexes bearing Schiff base ligands and evaluated their antitumor activity against HCC. They might be potential TrxR inhibitors which can effectively inhibit the overexpression of TrxR in HCC. In addition, the ion gold(III) which has a d^8 electronic configuration is isoelectronic with platinum(II) indicating gold(III) complexes hold promise as anticancer agents like cisplatin. Besides, these Schiff base ligands which are formed by the reaction of 1,2-bis(2-hydroxylphenyl)-1,2-diaminoethane and *p*-fluorobenzaldehyde have been capable of forming stable complexes with platinum and cobalt ions [28,29].

2. Results and discussion

2.1. Synthesis and characterization

Schiff base ligands **1a-4a** were synthesized from the corresponding diastereomerically pure 1,2-bis(2-hydroxyphenyl)-1,2-diaminoethane and two equivalents of *p*-fluorobenzaldehyde in the presence of ethanol [30]. Then, **1a-4a**, NH_4PF_6 and $NaAuCl_4{\cdot}2H_2O$ were mixed in a dichloromethane and ethanol solution under a nitrogen atmosphere to obtain complexes **1b-4b** (Scheme 1) [31].

The structures of Schiff base ligands **1a-4a** and gold(III) complexes **1b-4b** were characterized by NMR and MS spectra. It should be noted that there is a free rotation around the central C—C bond for our Schiff base ligands **1a-3a**. It leads to three staggered conformations: two structures with a gauche (**1a** and **2a**) and one with an anti-conformation (**3a**). The N—CH- protons of **1a** and **2a** showed a resonance in the ^{1}H NMR spectra at $\delta = 8.16$ compared to $\delta = 8.34$ in **3a**. The coordination of Schiff base ligands with gold(III), and the construction of square planar chelate complexes led to the complete disappearance of the resonance signals of the phenolic hydroxyl groups in the ^{1}H NMR spectra, which can characterize the compounds (Figs. S1a and b). This confirms the combination of oxygen with metal ions (C—O—Au). The resonance signals of the 1,2-diarylethane moiety and the signal of the N—CH- proton shifted in different directions. Those of the aromatic protons and the azomethine proton suffered a diamagnetic shift, while the ones at the ethane bridge are paramagnetic shifted.

The ^{13}C NMR spectra of **1a-3a** and **1b-3b** were also studied. Upon coordination of **1a-3a** with gold(III), the azomethine carbons as well as the fluorine bound carbons (F-C_{Ar}) suffered an upfield shift, while the CH resonances of **1b-3b** appeared at a lower field. These changes in the ^{13}C NMR were only minimal and different from the shifts observed in the ^{1}H NMR spectra. In addition, positive mode ESI mass spectrometry documented a base peak corresponding to the $[M\text{-}PF_6]^+$ fragment for gold(III) complexes **1b-4b**. Besides, the ^{1}H NMR spectra of **1b** did not change significantly within 7 days, indicating that gold(III) Schiff base complexes were relatively stable in DMSO-d_6/D_2O (V/V = 9: 1) (Fig. S2).

To gain insight into structural parameters and the coordination chemistry of gold(III) Schiff base complexes, crystals of **4b** was grown by slowly diffused methanol into a thick **4b** dichloromethane solution. As shown in Fig. 1, the gold atom of **4b,** which resides in a square-planar geometry, is four-fold coordinated via the azomethine nitrogen and the oxygen atom of the phenolic hydroxyl group. In addition, the space group of single crystals for **4b** is $Cmc2_1$, indicating that the stereochemistry of **4b** is a mixture of R,R-, or S,S-isomers (Table S1).

Besides, space coupling of chromophores in a chiral molecule gives rise to bisignate circular dichroism (CD) curves (Cotton effect) which enables one to determine absolute configuration and conformation of small molecules. To verify inversion of stereochemistry for the rearrangement reaction, selected compounds were determined by CD spectroscopy. As shown in Fig. S1c, there are strong cotton effects of the same amplitude but of opposite signs in ingredient **1a, 1b, 2a,** and **2b.** Thus, the CD spectra confirmed that the stereostructure of **1b** and **2b** is different.

2.2. Reaction with glutathione (GSH) and N-acetylcysteine (NAC)

Next, we further examined the stability of the gold(III) Schiff base complex in the presence of biological thiols. As shown in the Fig. S3A, when **1b** was treated with equivalent GSH, the UV absorption curve changed significantly, indicating the existence of reactions between **1b** and GSH. The interaction of **1b** with NAC was also investigated (Fig. S3B). When **1b** was treated with NAC for 24 h, the peak at 2.9 ppm (-S—CH_2—) was split. In addition, the formation of a yellow precipitate was observed within 10 min after dissolving in NAC. It can be seen that **1b** can still react with it although the reduction potential of NAC is much higher than that of GSH, suggesting that the oxidation reaction has occurred. Therefore, we speculated that **1b** can interact with mercapto biomacromolecules and have a certain oxidation property. Gold(III) may be reduced to gold(I) by reductive substances such as GSH *in vivo*.

2.3. In vitro antiproliferative activity

Initially, the antiproliferative activity of **1b-4b** and the selected intermediate **1a** against human HCC cells (HepG2, SMMC-7721 and Hep3B) were tested by MTT assay after 72 h incubation, cisplatin and auranofin were used as the positive control. As expected, similar to cisplatin and auranofin, low IC_{50} values (5.4—12.1 μM) of **1b-4b** for the cytotoxicity assay were reached against HCC cells. It should be noted that the stereoisomerization of the 1,2-diimino-1,2-diarylethane bridge did not affect their antitumor activity much. The inactivity (IC_{50} values > 20 μM) of the Schiff base ligand **1a** indicated that the gold center of **1b** was important to obtain its bioactive species.

As outlined in Table 1, HepG2 cell line was the most sensitive to **1b** with an IC_{50} value of 5.40 μM compared to other HCC (SMMC-7721 and Hep3B) cell lines. Further, we investigated the cytotoxicity of **1b** in other cancer cells (MCF-7 and HT-29). **1b** showed higher IC_{50} values in MCF-7 (IC_{50}: 10 μM) and HT-29 (IC_{50}: 10.81 μM) than in HepG2 cells (Fig. S4A).

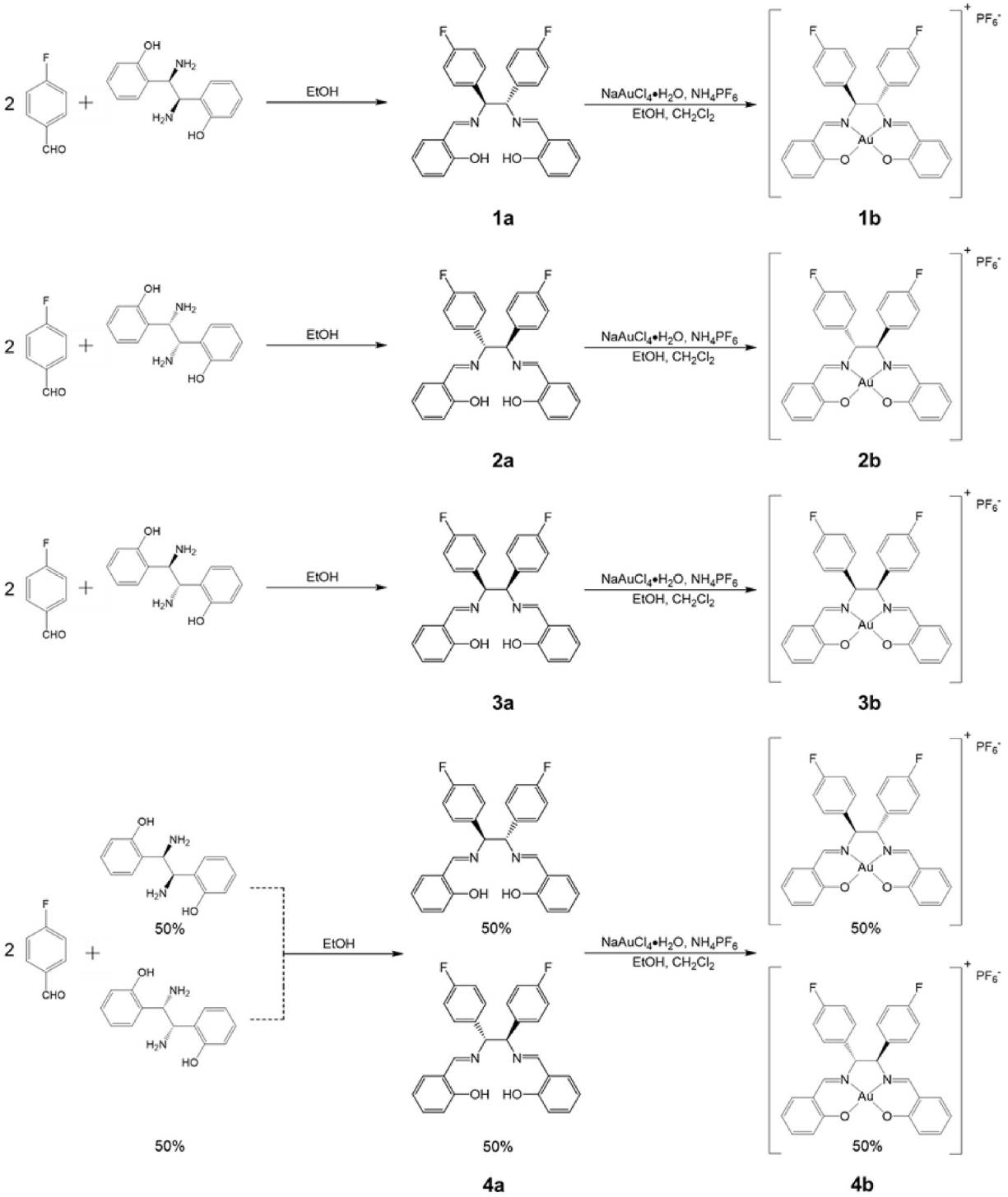

Scheme 1. Synthesis of gold(III) complexes **1b-4b**.

To obtain the safe dose of **1b** for further study, we tested the cytotoxicity of **1b** in a normal liver cell line (LO_2). Interestingly, **1b** exhibited a slight selectivity towards tumor (5.40 μM in HepG2 cells) over non-tumor cell lines (10.28 μM in LO_2 cells) (Fig. S4B). ALT and LDH release are seen as important indicators of cell membrane integrity and are widely used for cytotoxicity testing, so we evaluated the ALT and LDH levels of **1b** in LO_2 cells. 10 μM of **1b** caused minimal harm to normal cell (Figs. S4C and D). In other words, these doses (2.5 μM, 5 μM, 10 μM) are safe in the follow up studies.

2.4. Interaction with TrxR

As mentioned above, the selenoenzyme TrxR has been considered to be a putative target for gold complexes. Thus, we studied the TrxR inhibitory of **1b** on isolated enzyme using the DTNB assay. Interestingly, the activity of purified TrxR was dramatically inhibited by **1b** (IC_{50} = 0.37 μM) (Fig. 2A), suggesting TrxR as a possible biological target for **1b**. This complex is comparably active as most of gold complexes such as gold *N*-heterocyclic carbene complexes,

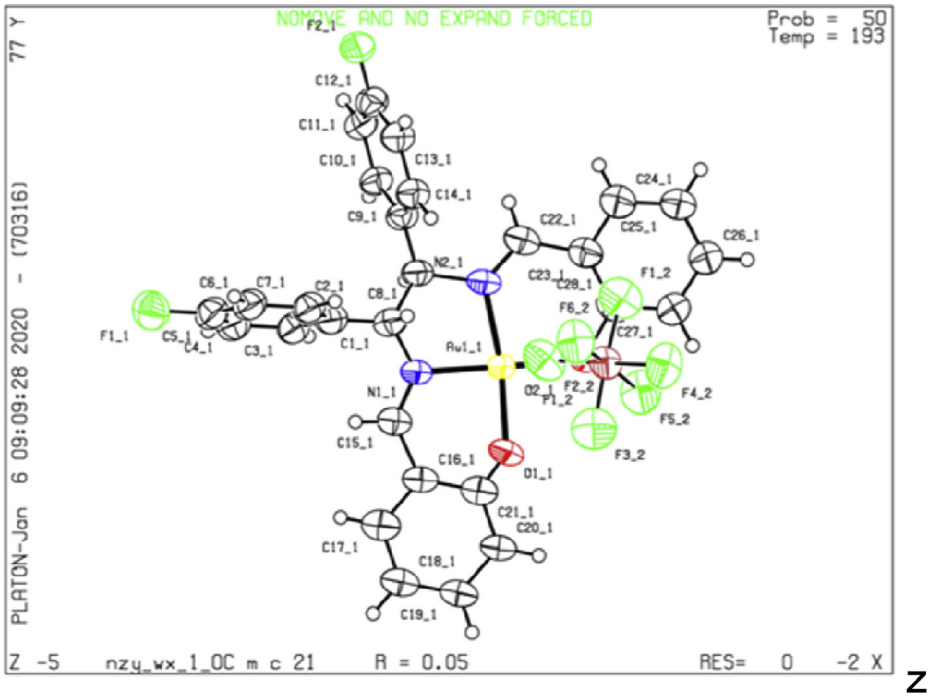

Fig. 1. X-ray crystal structure conformation of **4b**.

Table 1
The antiproliferative activity of **1b-4b** against HepG2, SMMC-7721 and Hep3B cell lines (n = 3, IC_{50} values, mean ± SD [μM]).

Compounds	HepG2	SMMC-7721	Hep3B
1b	5.40 ± 0.99	10.05 ± 1.19	10.89 ± 1.26
2b	7.50 ± 0.77	10.17 ± 1.88	12.01 ± 1.82
3b	10.29 ± 1.14	8.25 ± 1.29	9.03 ± 1.26
4b	6.49 ± 0.89	9.45 ± 1.89	9.48 ± 1.86
1a	>20	>20	>20
Cisplatin	1.42 ± 0.21	2.76 ± 0.41	1.32 ± 0.14
Auranofin	1.74 ± 0.32	2.24 ± 0.24	1.93 ± 0.21

but slightly less active than auranofin (IC_{50} = 82.6 nM) [32]. It should be mentioned that though auranofin has the good inhibitory effect in TrxR, it showed the rapid metabolization and conjugated to serum proteins before reaching the target enzyme [19,24,33,34]. In addition, these gold(III) complexes may act through a different mechanism such as oxidative damage to the enzyme [35].

Next, we measured the TrxR inhibitory activity of **1b** in HepG2 cells. In this assay, **1b** showed a TrxR inhibitory activity (with an IC_{50} = 6.51 μM) (Fig. 2B), showing that it may represent a fresh kind of TrxR inhibitor with potential for the further research. Besides, we also evaluated the mRNA levels of TrxR by real-time PCR analysis after treatment of **1b** (2.5 μM, 5 μM, and 10 μM) for 24 h in HepG2 cells. As shown in Fig. 1C, **1b** reduced TrxR activity in HepG2 cells. The immunofluorescence and Western blot analysis further confirmed these alterations (Fig. 2D–E). The TrxR expression was highly expressed in control (DMSO), and the expression was dose-dependently decreased after treatment with **1b**. Overall, all these results confirmed that the selenoprotein TrxR could be a possible target for our gold(III) Schiff base complexes.

2.5. *1b induced HepG2 cells apoptosis by mitochondrial dysfunction and ROS production*

Gold complexes have been reported to bring out computable mitochondrial dysfunction, and cause cancer cell death through inhibiting TrxR activity [15,22,36]. Therefore, we used the JC-1 kits to test the mitochondrial membrane potential (MMP) with the treatment of **1b** (2.5 μM, 5 μM, and 10 μM). After treated HepG2 cells with **1b** for 24 h, the green (monomeric) fluorescence was increased compared to the control (DMSO) (Fig. 3A), indicating that the mitochondrial dysfunction might be important in death processing.

The damage of mitochondrial could cause the increase of ROS [37]. The imbalanced ROS after treated with **1b** (2.5 μM, 5 μM, and 10 μM) for 24 h in HepG2 cells triggered cellular dysfunction consequently (Fig. 3B). Then, the ability of **1b** to induce nuclear apoptosis morphology was further detected by Hoechst 33258 staining (Fig. 3C). The nuclei of HepG2 cells appeared hyper condensed (brightly stained) in **1b**-treated group. In addition, trypan blue staining revealed that **1b** induced HepG2 cells death dose-dependently (Fig. 3D). These results indicated that **1b** could impair mitochondrial function effectively and induce the strong apoptosis in HepG2 cells.

2.6. *1b-induced cells arrest in G2/M and apoptotic pathways*

The effect of **1b** (2.5 μM, 5 μM, and 10 μM) on cell cycle progression was further investigated. The proportion of cells that accumulated in the G2/M phase increased compared to the G0/G1 and S phases after treated with **1b** for 72 h (Fig. 4A and B). Interestingly, as shown in Fig. 4C and D, the expression cycle-related proteins' levels of G2/M phase (Cyclin A and CDK2) were significantly reduced after treatment of **1b** (10 μM) compared to the DMSO control.

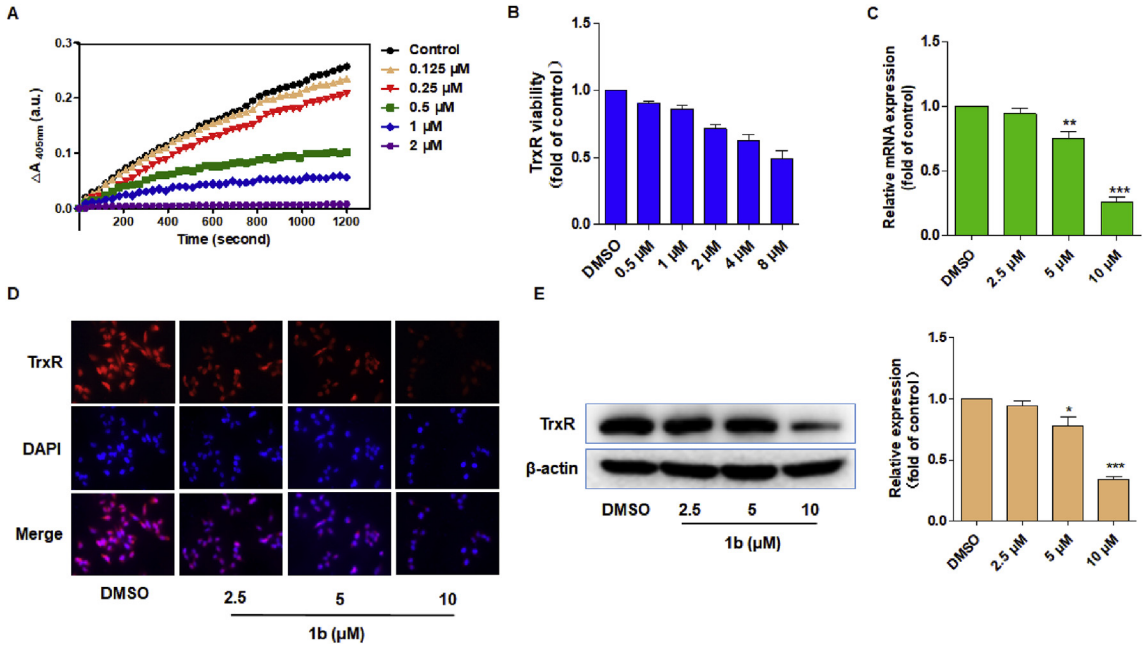

Fig. 2. **1b** inhibited the expression of TrxR. (A) Inhibition of the purified TrxR by **1b**. (B) Quantification of TrxR activity in HepG2 cells treated with **1b** at 37 °C for 24 h. (C) mRNA level of TrxR in HepG2 cells treated with **1b**. (D) Immunofluorescence analysis of TrxR (original magnification, 40 ×). (E) Western blot analysis of TrxR. Error bars: S.D., n = 3. Statistical significance of differences in mean values: *p < 0.05, **p < 0.01 and ***p < 0.001.

In addition, the percentage of apoptotic cells was dose-dependently increased after treatment with **1b** for 72 h (Fig. 5A and B). The number of apoptotic cells in **1b** (10 μM) treatment is the highest compared to other group. Besides, **1b** increased the expression of the pro-apoptosis proteins AIF, cytochrome *c* and cleaved-PARP/PARP (Fig. 5C and D). The level of apoptotic marker (AIF) by immunofluorescence analysis is consistent with Western blot (Fig. 5E). Collectively, these data supported that the inhibition of HepG2 proliferation and promotion of apoptosis were significant in anti-HCC.

2.7. *1b* activated endoplasmic reticulum stress (ERS) in HepG2 cells

Next, we studied the further mechanism of downstream signaling molecules involved in **1b**-induced mitochondrial activation. Gold(III) complex was recently reported to display cytotoxicity through ER damage [38,39]. Thus, we tested the intracellular ROS and ERS in HepG2 cells. It was noticed that a clear colocalization of ROS with the ER after incubating with **1b** (2.5 μM, 5 μM, 10 μM). The **1b** could significantly increase the fluorescence level, and activate the colocalization of ROS and ERS dose-dependently (Fig. 6A). Thus, the activation of ROS is accompanied by the ERS activation, and it is extremely possible owing to the increased the membrane permeability of ER after the drug stimulation.

To find the interesting pro-apoptotic pathway activated by **1b** in HepG2 cells, we tested the ERS-induced cancer cell apoptosis, which becomes a novel signaling target. As shown in Fig. 6B and C, C/EBP homologous protein (CHOP) and Calnexin, which are an ER chaperone and a major marker of prolonged ERS respectively, were up-regulated after treating HepG2 cells with **1b** for 24 h. It is indicated that **1b** could activate the ERS in HepG2 cells effectively. The level of protein by Western blot is consistent with immunofluorescence analysis (Fig. 6D and E). All these results showed that gold(III) complex **1b** could induce ROS led to the activation of a lethal ERS, at least partly contributing to the apoptosis in HepG2 cancer cells.

2.8. Activation of ERS and ROS is required for *1b* to reduce the TrxR level in HepG2 cells

To explore whether ROS and ERS play an important role in **1b**-induced apoptosis in HepG2 cells, we used the ERS-specific inhibitor salubrinal (Sal) (10 μM) and ROS-specific scavenger NAC (2 mM) to inhibit the expression of ERS and ROS respectively. It was observed that **1b** inhibited the TrxR level by immunofluorescence analysis, while Sal and NAC treatment can counteract this effect observably (Fig. 7A and B). Western blot analysis is consistent with the results (Fig. 7C and D). As high ROS levels can trigger the rupture of mitochondrial membrane, we further surmised whether inhibiting ERS activation could facilitate the TrxR expression. Results indicated that **1b** (5 μM) could efficiently reduce the viability of TrxR, however, this effect can be counteracted by treatment with Sal (10 μM) obviously (Fig. 7E). Following, we used the NAC to offset the generous accumulation of ROS. From the PCR analysis, **1b** reduced the TrxR activity, and NAC treatment was opposite trend compared with **1b** treatment (Fig. 7F). Subsequently, we explored whether the ROS accumulation in the ER domain induced the activation of ERS. Pretreatment of HepG2 cells with NAC, we found specific ROS clearance in cells against **1b** induced cell death through ERS, the markers of ERS (CHOP and Calnexin) were all high expressions in **1b** treatment and reversion by NAC (Figs. S5A and B). Western blot analysis is consistent with the results (Figs. S5C and D). Accordingly, our studies clearly demonstrated that the biological action of **1b** in HepG2 cells is reliant on its interaction with TrxR and ERS.

2.9. Interaction with DNA

DNA symbolizes a primary target for anticancer metal complexes including gold complexes [40–42]. Thus, we studied the DNA binding to identify the binding of our gold(III) Schiff base complex **1b** with the calf thymus DNA (CT-DNA). With the DNA concentration increased, the absorption of 1b has an obvious

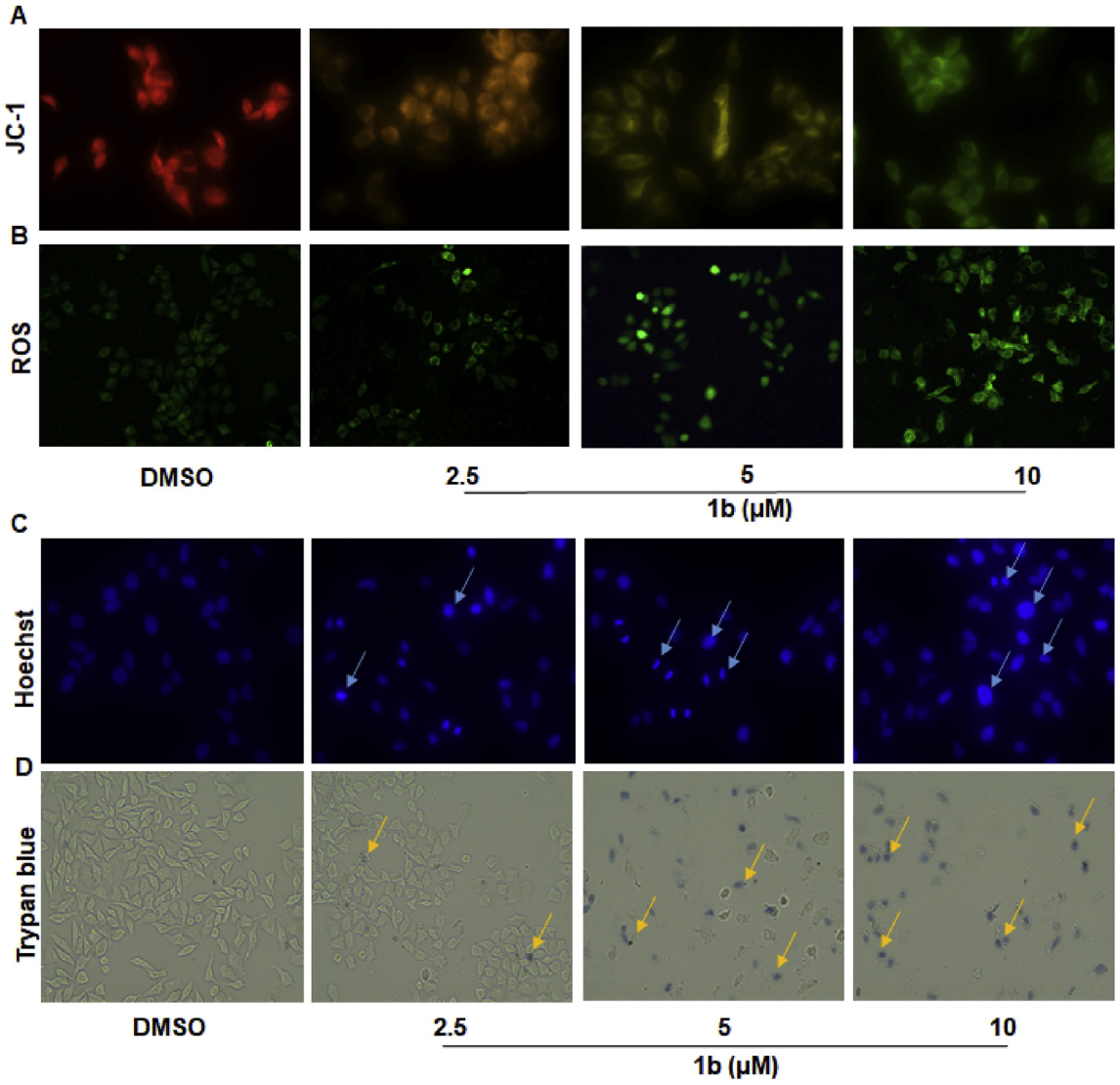

Fig. 3. **1b** induced mitochondrial dysfunction and cells damage. (A) Mitochondrial membrane damage imaged by JC-1 staining treated with **1b**. (B) ROS positive cells treated with **1b** in HepG2 cells (original magnification, 40 ×). (C, D) Hoechst 33258 staining (original magnification, 40 ×) and Trypan blue staining (original magnification, 20 ×) treated with **1b** for 24 h in HepG2 cells. (For interpretation of the references to colour in this figure legend, the reader is referred to the Web version of this article.)

hyperchromicity indicating that there may be a hydrogen bonding action between CT-DNA and 1b (Fig. S6). Next, we investigated DNA conformational changes induced by 1b in PBS buffer solution (pH = 7.2) at various ratios (r_b = [**1b**]/[DNA] of 0.0, 0.02, 0.05, 0.1) by CD spectroscopy. Interestingly, the positive CD signal was remarkably reduced at 273 nm. These may show π−π interactions between the DNA nucleobases and the π-system of **1b**, which need further research to prove.

2.10. *1b improves liver damage and tumor microenvironment in vivo*

A great deal of animal models provide relevant information on the pathogenesis of HCC [43–45]. Chronic treatment with carbon tetrachloride (CCl_4) is a mature method to induce liver cancer [4,45–47]. Hence, to further assess the anti-HCC activity of **1b** *in vivo*, we chose CCl_4-induced chronic HCC mice. Intraperitoneal injection CCl_4 into the mice for 16 weeks induced chronic liver injury which led to pathological morphological changes in liver, including inflammation, steatosis, and necrosis.

At the sixteenth week, mice liver in model group turned yellowish-tan with diffuse uniform micronodules separated by fibrous septa. Steatosis, severe centrilobular necrosis, porto-portal and porto-central bridging fibrosis, rearrangement of blood circulation and pseudolobule with macrophage infiltration were observed in the model group. All animal livers dealt with CCl_4 had cirrhotic features, which indicated that the liver cirrhosis model was successfully modeled (Figs. S8 and 8A). To test the protective effect of **1b** (20 mg/kg), we analysed biochemical markers of liver injury after CCl_4 treatment. H&E staining showed that treatment with 20 mg/kg of **1b** significantly ameliorated the morphological changes in liver tissue. However, normal liver lobule destruction, altered hepatic foci, hepatocellular edema, steatosis and marked nuclear polymorphism in H&E staining were still observed in CCl_4 group (Fig. 8A). Collagen accumulation accompanies fibrogenesis, therefore, liver tissue sections were stained with Masson's and Sirius red reagent to examine collagen expression in the mouse liver. These results showed that collagen was obviously increased in the CCl_4-injured liver but was decreased in the **1b** treatment group (Fig. 8B and C). The levels of liver injury factors, AST, ALT and LDH,

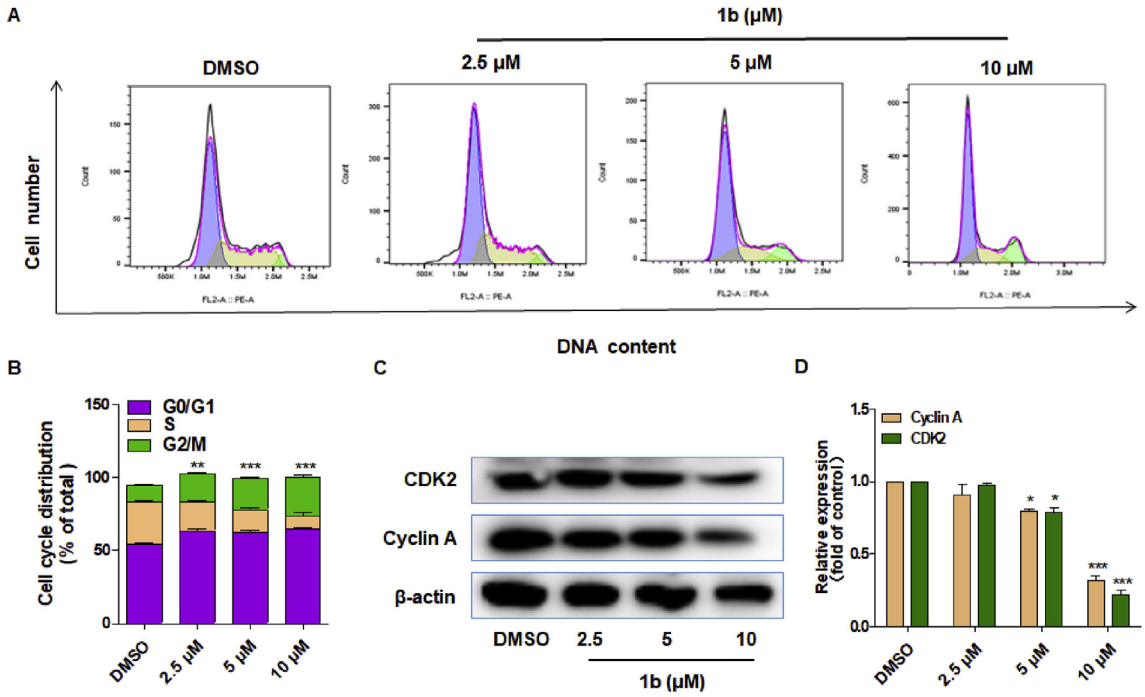

Fig. 4. **1b**-induced cells arrest in G2/M. (A, B) Effects of **1b** on cell cycle progression. (C, D) Western blot analysis of HepG2 cells after treatment with **1b** for 24 h. Error bars: S.D., n = 3. Statistical significance of differences in mean values: *p < 0.05, **p < 0.01 and ***p < 0.001.

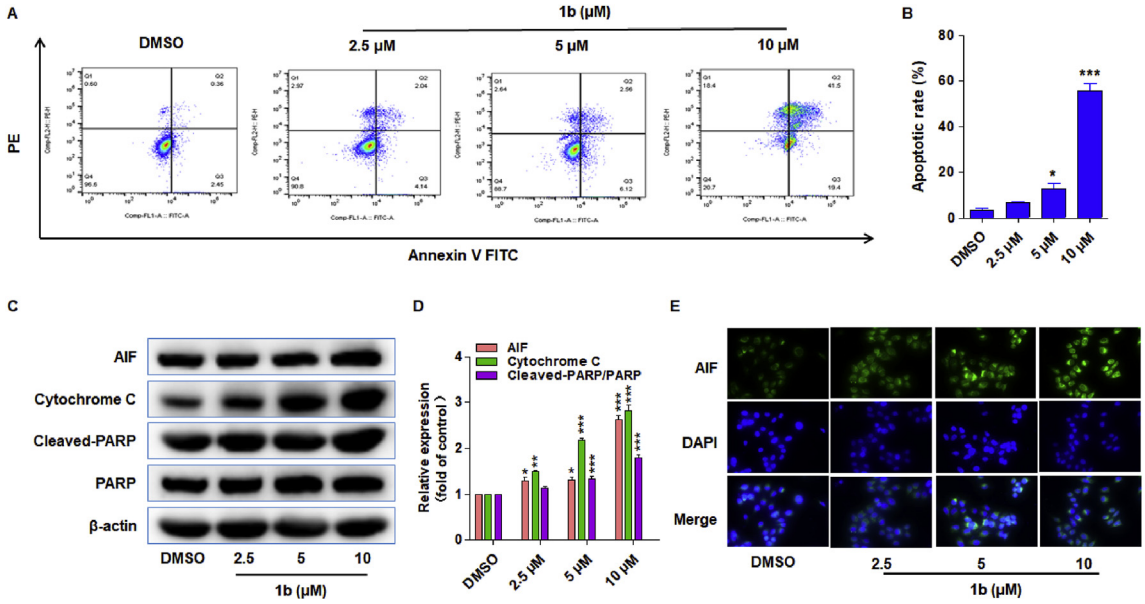

Fig. 5. **1b**-induced apoptotic pathways. (A, B) Apoptosis of HepG2 cells treated with **1b** for 72 h. (C, D) Western blot analysis of HepG2 cells treated with **1b** for 24 h. (E) The expression of apoptosis-inducing factor (AIF) by immunofluorescence analysis in HepG2 cells after treatment with **1b** for 24 h (original magnification, 40 ×). Error bars: S.D., n = 3. Statistical significance of differences in mean values: *p < 0.05, **p < 0.01 and ***p < 0.001.

were effectively increased in the CCl_4 model group and decreased by **1b** treatment group (Fig. 8D). Interestingly, H&E staining analysis further indicated nontoxicity in mouse hearts, spleens, lungs and kidneys at the dose of 20 mg/kg (Fig. 8E). Taken together, these results can provide more *in vivo* evidence that treatment of **1b** did reduce the accumulation of collagen and inhibit the inflammation in HCC model mice.

During chronic liver disease, inflammation is commonly accompanied by hepatocellular injury [48]. Inflammatory cells and regulatory factors are present in the microenvironment of most liver injury. The inflammatory microenvironment has direct mutagenic effects [49]. As NFκB pathway plays an essential role connecting inflammation and cancer, we tested the expression of NFκB using Western blot and immunofluorescence analyses. It shows that the higher NFκB level in model group than **1b** treatment group, indicating that NFκB pathway was activated during hepatocarcinogenesis (Fig. 9A and B). In addition, severe inflammatory cell infiltration in livers exposed to CCl_4 was suppressed by **1b**, as

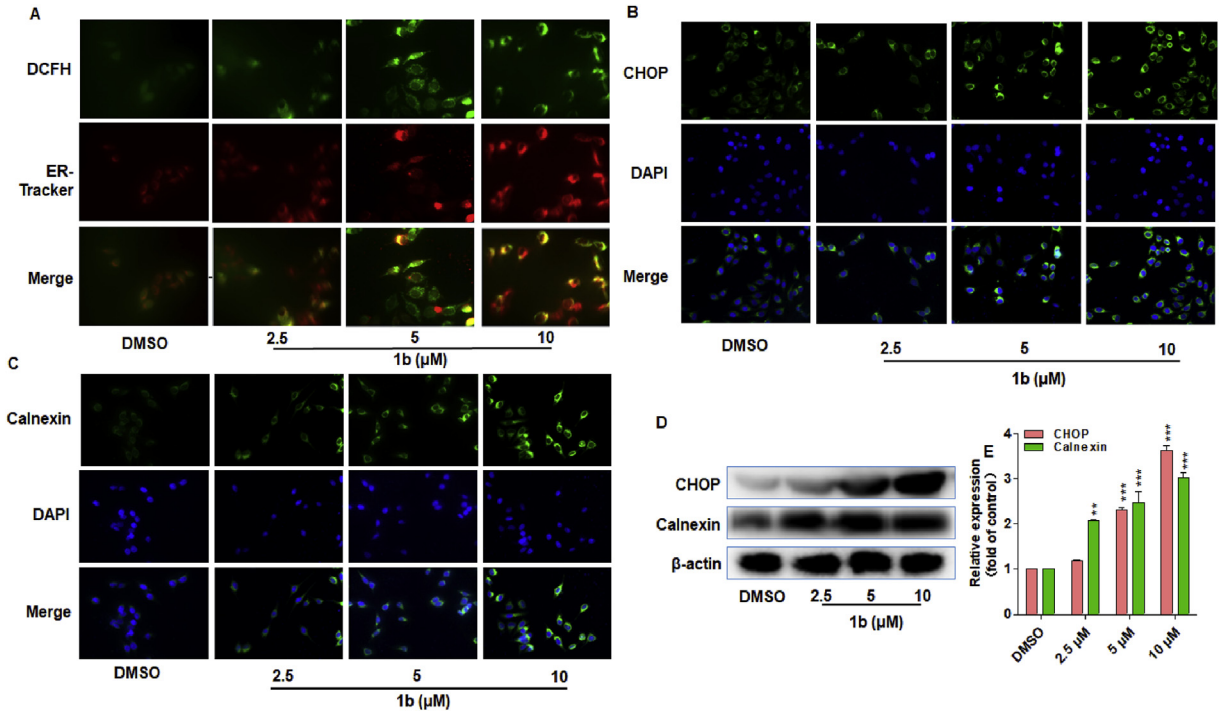

Fig. 6. **1b** induced the activation of ERS in HepG2 cells. (A) Immunofluorescence analysis of cells treated with **1b** for 24 h, and incubation with DCFH (ROS indicator, green) and ER-Tracker red (Red) (original magnification, 40 ×). (B, C) The expression of ERS marker factors (CHOP and Calnexin) by immunofluorescence analysis treated with **1b** for 24 h (original magnification, 40 ×). (D, E) The expression of ERS-inducing factor by Western blot treated with **1b** for 24 h. Statistical significance of differences in mean values: *p < 0.05, **p < 0.01 and ***p < 0.001 (n = 3). (For interpretation of the references to colour in this figure legend, the reader is referred to the Web version of this article.)

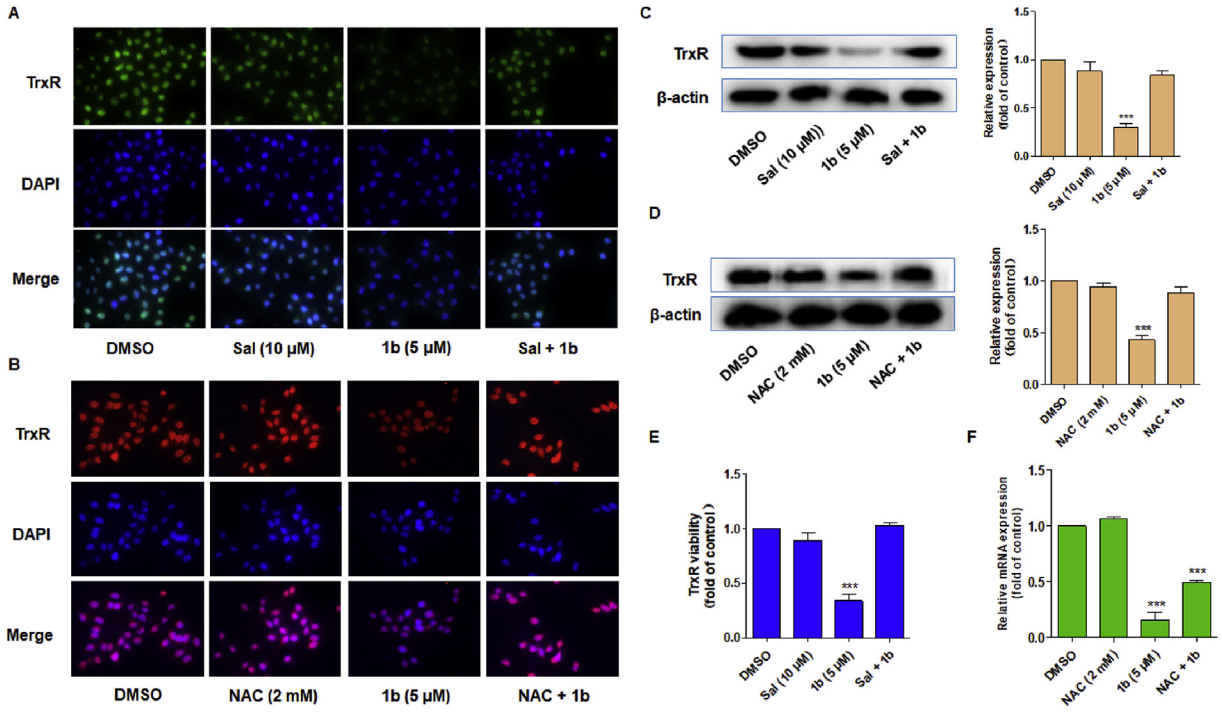

Fig. 7. Activation of ERS is required for **1b** to induce HepG2 cells apoptosis. (A) Immunofluorescence analysis in HepG2 cells treated with **1b** and Sal at 37 °C for 24 h (original magnification, 40 ×). (B) Immunofluorescence analysis in HepG2 cells treated with **1b** and NAC at 37 °C for 24 h (original magnification, 40 ×). (C, D) Western blot assays in HepG2 cells. (E) Quantification of TrxR activity in HepG2 cells treated with **1b** and Sal at 37 °C for 24 h. (F) mRNA level of TrxR in HepG2 cells treated with **1b**. Error bars: S.D., n = 3. Statistical significance of differences in mean values: *p < 0.05, **p < 0.01 and ***p < 0.001.

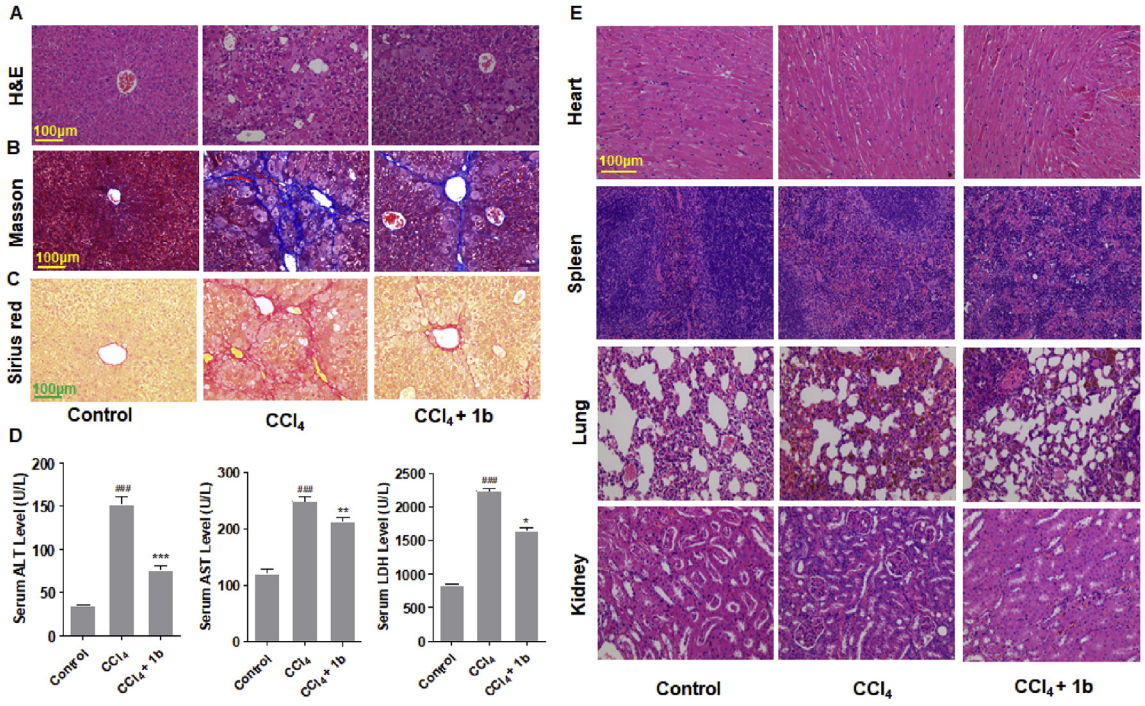

Fig. 8. 1b decreased the collagen accumulation and improved liver injury *in vivo*. (A) Liver issue conventional slice with H&E staining. (B, C) Liver issue conventional slice with Masson and Sirius red staining after treatment with control, CCl_4, and both CCl_4 and **1b**. (D) Determination of serum ALT, AST and LDH levels after treatment with control, CCl_4, and both CCl_4 and **1b**. (E) HE staining of the major organs (Original magnification, 20 ×). For the statistics of each panel in this figure, data are expressed as mean ± SD (n = 6); ###p < 0.001 compared with control, *p < 0.05, **p < 0.01 and ***p < 0.001 compared with group CCl_4. (For interpretation of the references to colour in this figure legend, the reader is referred to the Web version of this article.)

characterized by a decrease in the number of TNFα and IL-1β. Immunohistochemistry and immunofluorescence analysis showed that **1b** treatment could improve the inflammation level in CCl_4 model group (Fig. 9C–F). Thus, **1b** treatment could improve inflammation microenvironment and relieve liver injury.

Furthermore, we examined the effects of TrxR which is expressed in inflamed sites might be involved in inflammatory reactions via NFkB activation [50]. Immunohistochemistry and immunofluorescence analysis were further tested to confirm the level of TrxR, the expression of TrxR was high in CCl_4-injured liver, and treatment with **1b** significantly reversed these changes (Fig. 10A and B). In liver tissue and serum, the analysis is consistent with the results in immunohistochemistry and immunofluorescence analyses (Fig. 10C–E). Overall, these results can provide some evidences that treatment of gold(III) Schiff base complex **1b** could improve the CCl_4 induced the liver damage by down-regulation of TrxR expression and inflammation level in HCC model mice.

3. Conclusion

In summary, a series of gold(III) Schiff base complexes were synthesized and exhibited very promising anti-HCC activity. Among them, the most active complex **1b** has a strong effective TrxR inhibitory activity both *in vitro and in vivo*. As shown in Fig. 11, the most active gold(III) Schiff base complex **1b** targets TrxR to induce ROS in HepG2 cells and finally activate ROS-dependent ERS activation. Eliminating the ERS by the inhibitor Sal totally abolished the anticancer effects. Moreover, excessive accumulation of ROS can lead to mitochondrial dysfunction. In other words, **1b**-induced ERS is a secondary response to **1b**-induced ROS and it could overstate the cell death instead of being a mediator in HCC cells. The considerable ROS release and TrxR inhibition of **1b** induced a prominent ERS response. Besides, **1b** treatment was able to prevent hepatocarcinogenesis and progression in mice models. In our study, this complex could improve the CCl_4-induced liver damage and inflammation level. Thence, **1b** may represent a novel gold-based TrxR inhibitor and a potential candidate for the treatment of HCC.

4. Experimental section

4.1. General materials and instrumentations

All reagents were obtained commercially and were used without further purification. Solvent was dried and used according to standard procedures. All chemical reactions were monitored by TLC. Deuterated solvents were purchased from Cambridge Isotope Lab Inc. (CIL). Solutions for all spectroscopic and biological studies were prepared with solvents of HPLC grade and doubly distilled water from Millipore (>18.2 MΩ). Antibodies, such as TrxR were purchased from Proteintech Co. (China), AIF and β-actin were purchased from Wuhan Sevier Biotechnology Co. (China). JC-1 assay kits were purchased from KeyGen Co. (China); ROS assay kit, ATP assay kits and all secondary antibodies were purchased from Beyotime Biotechnology (China). TrxR activity assay kits were purchased from Solarbio (Beijing), purified TrxR (rat liver) was purchased from Sigma-Aldrich Co. Antibodies against Calnexin and CHOP were purchased from Wan Lei Biology Antibody (China). The primers used in PCR were purchased from GenScript Co. Ltd. (China). PBS, Dulbecco's Modified Essential Medium (DMEM) and trypsin-EDTA were bought from GIBCO BRL (USA).

^1H and ^{13}C NMR data were acquired on a Bruker AV-500. HPLC data were recorded on a Waters Arc. UV-2401PC spectrophotometer was used for recording electronic absorption spectra. CD spectra were recorded on circularly polarized fluorescence spectrometer CPL 300. Fluorescent microscopy was performed using a Leica DMi8 fluorescence microscope. ESI-MS spectra were obtained

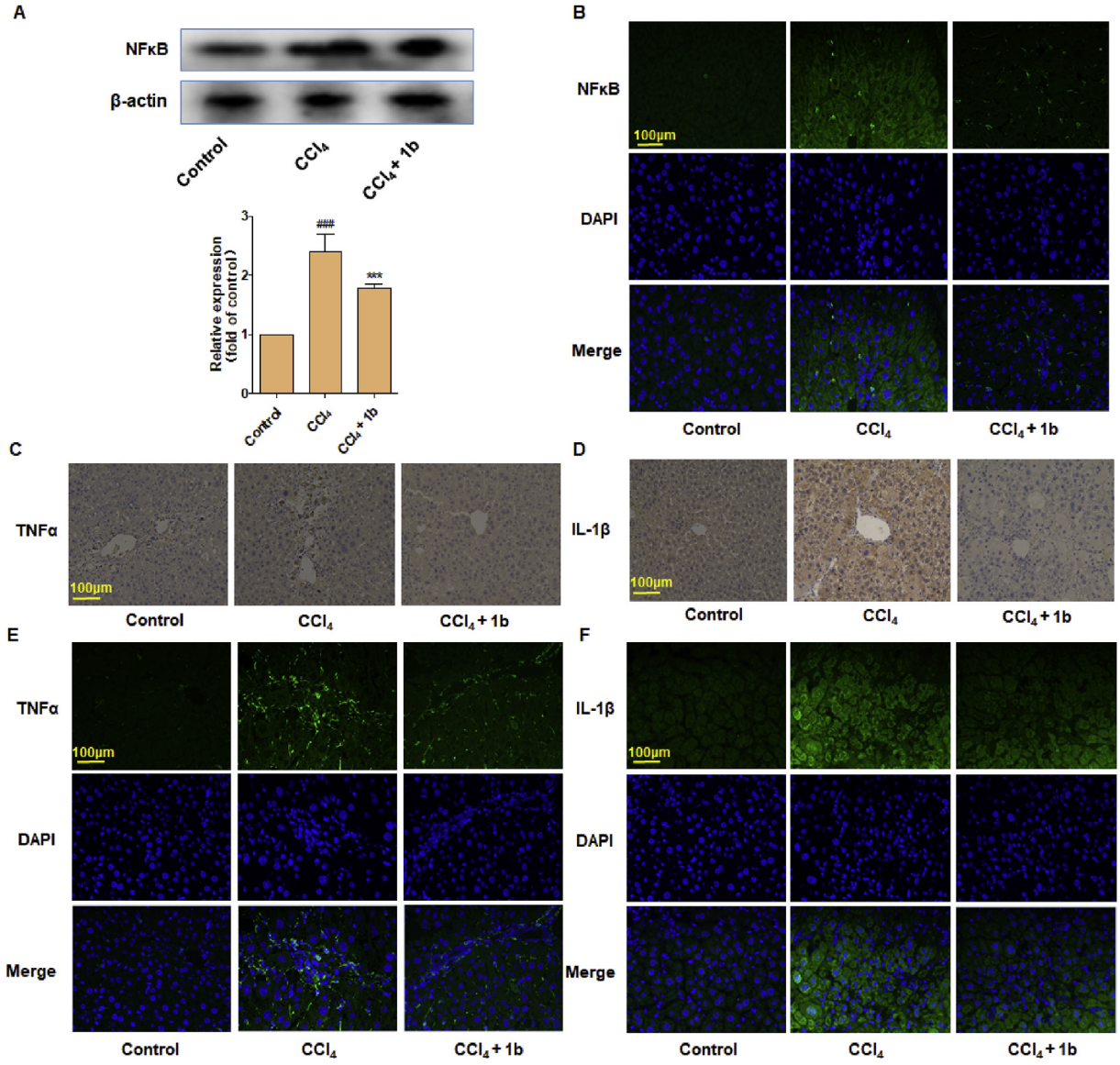

Fig. 9. 1b improved inflammation microenvironment to relieve liver injury. (A, B) Tumor tissues were tested with Western blot and stained with immunohistochemistry. (C, D) Tumor tissues were stained with immunohistochemistry using antibodies against TNFα and IL-1β (Original magnification, 20 ×). (E, F) Tumor tissues were stained with immunofluorescence using antibodies against TNFα and IL-1β. DAPI to stain the nucleus (Original magnification, 40 ×). Scale bar = 100 μm. For the statistics of each panel in this figure, data are expressed as mean ± SD (n = 6); $^{###}p < 0.001$ compared with control, $^{*}p < 0.05$, $^{**}p < 0.01$ and $^{***}p < 0.001$ compared with group CCl_4.

by Agilent 6125 and HRMS spectra were acquired on Agilent 6210 ESI-TOF. Flow Cytometer was BD C6 Plus. MTT and protein assays were quantified by Perkin-Elmer Fusion Reader (Packard BioScience Company). X-Ray Single Crystal Diffractometer was BRUKER Smart APEX II CCD. The purity of the target compounds was evaluated using HPLC proving ≥ 95% purity.

4.2. Synthesis and characterization

4.2.1. General procedure for the synthesis of Schiff base ligand *1a-4a*

2.4 mmol of *p*-fluorobenzaldehyde was added to a cloudy solution of 220 mg (1 mmol) of 1,2-bis(2-hydroxylphenyl)-1,2-diaminoethane in 3.3 mL of ethanol. The clear reaction mixture was stirred for 12 h at room temperature to give **1a-4a** as a yellow precipitate. The yellow precipitate was filtered, washed with 10 mL of ethanol, and dried in vacuum.

4.2.2. General procedure for the synthesis of gold(III) Schiff base complexes *1b-4b*

A solution of NH_4PF_6 (0.14 mmol) in EtOH (1 mL) was added to a suspension of $NaAuCl_4 \bullet 2H_2O$ 0.05 (mmol) in CH_2Cl_2 (1 mL). After the dropwise addition of a solution of Schiff base ligands **1a-4a** (0.2 mmol) in CH_2Cl_2 (1 mL), the reaction mixture was stirred for 24 h. Then, hexane was added to the action mixture to induce precipitation. The precipitate was collected and washed with chloroform. The collected precipitate was dissolved in CH_3CN and filtered. The filtrate was concentrated under reduced pressure and dried in vacuum to give gold(III) Schiff base complexes **1b-4b**.

2,2'-((1E,1′E)-(((1S,2S)-1,2-bis(4-fluorophenyl)ethane-1,2diyl) bis(azanylylidene))bis(methanylylidene))diphenol (**1a**). Yield 69%; Yellow solid; ^{1}H NMR (500 MHz, $CDCl_3$) δ 13.13 (s, 2H), 8.34 (s, 2H), 7.35−7.26 (m, 2H), 7.20−7.11 (m, 6H), 6.96 (dd, J = 17.7, 8.7 Hz, 6H), 6.84 (t, J = 7.5 Hz, 2H), 4.69 (s, 2H).^{13}C NMR (126 MHz, $CDCl_3$) δ 166.41, 163.10, 161.14, 160.82, 134.96, 132.82, 131.86, 129.36,

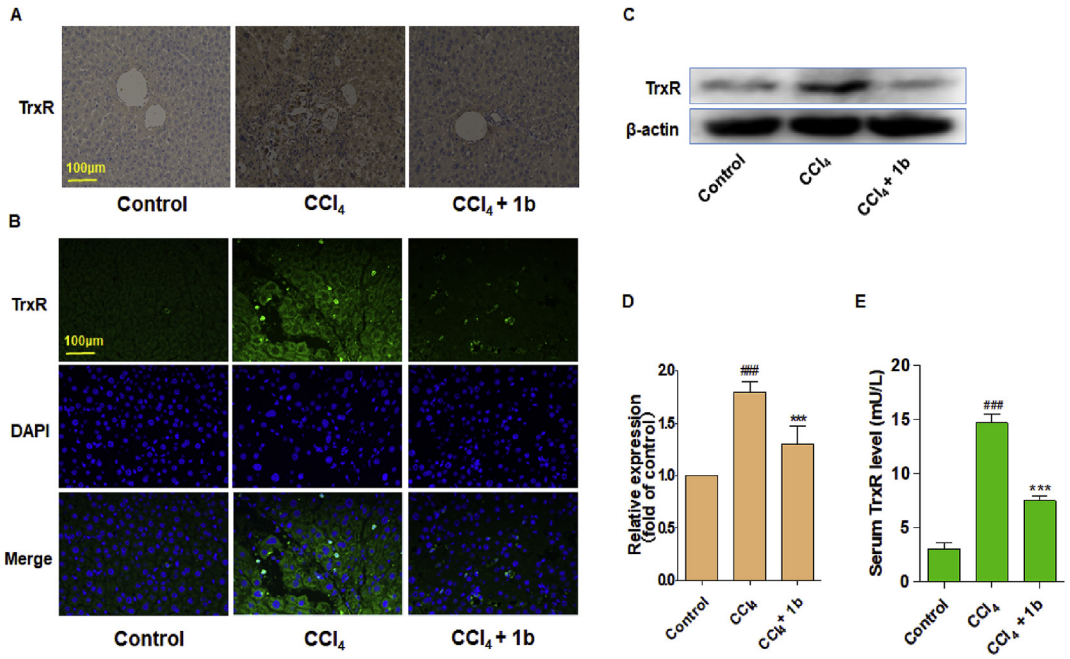

Fig. 10. 1b decreased TrxR activity *in vivo*. (A, B) Tumor tissues were stained with immunohistochemistry and immunofluorescence using antibodies against TrxR. (C, D) Western blot analysis on the expressions of TrxR. β-actin was used as protein loading control. (E) ELISA measurement of TrxR levels in serum. For the statistics of each panel in this figure, data are expressed as mean ± SD (n = 6); ###p < 0.001 compared with control, ***p < 0.001 compared with group CCl_4.

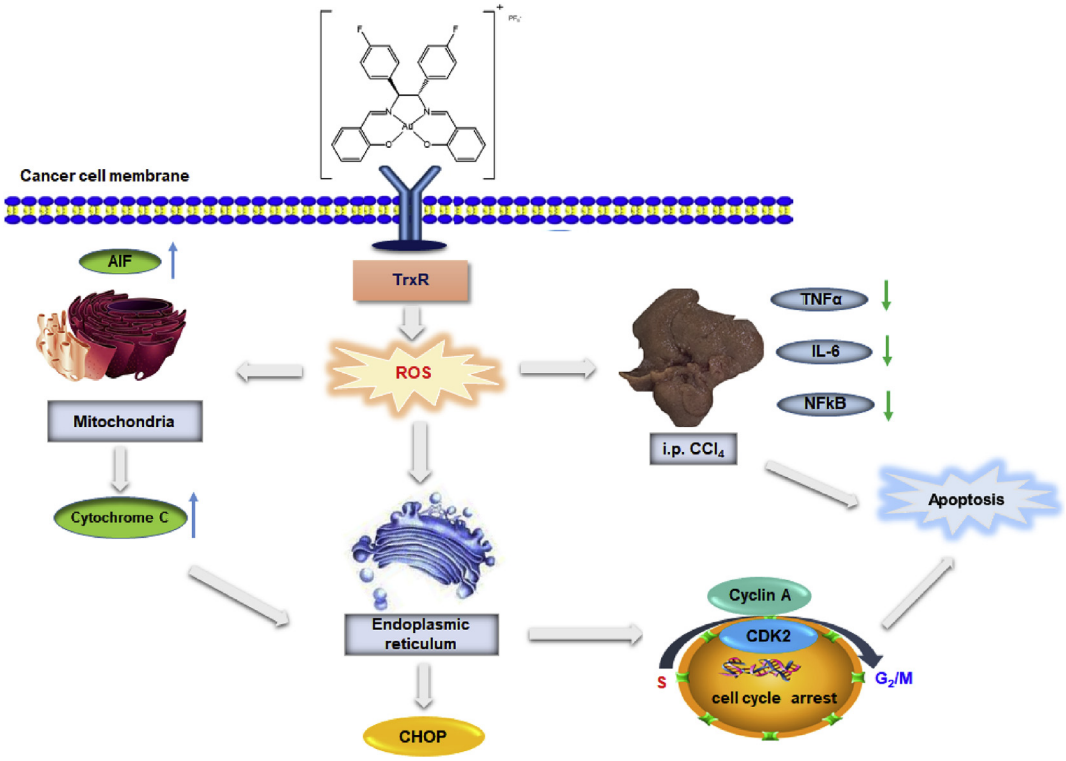

Fig. 11. Proposed anticancer mechanisms of **1b**.

118.93, 118.43, 116.93, 115.49, 115.32, 79.54. ESI-MS: 457.2 ($[M+H]^+$).

[2,2'-((1E,1'E)-(((1S,2S)-1,2-bis(4-fluorophenyl)ethane-1,2-diyl) bis(azanylylidene))bis(methanylylidene))diphenol]gold(III) hexafluorophosphate (**1b**). Yield 16%; Red solid; ^{1}H NMR (500 MHz, CD_3CN) δ 7.97 (s, 2H), 7.79 (ddd, *J* = 8.7, 7.0, 1.7 Hz, 2H), 7.58 (dd, *J* = 8.1, 1.6 Hz, 2H), 7.48–7.40 (m, 4H), 7.34 (d, *J* = 8.6 Hz, 2H), 7.23 (dd, *J* = 12.2, 5.4 Hz, 4H), 7.05–6.96 (m, 2H), 5.74 (s, 2H).^{13}C NMR (126 MHz, CD_3CN) δ 164.77, 162.79, 160.86 , 140.10, 136.48, 132.19, 127.20, 119.89, 119.02, 118.14 , 116.93, 116.75, 80.08. ESI-MS: 651.0

($[M\text{-}PF_6]^+$).

2,2'-((1E,1′E)-(((1R,2R)-1,2-bis(4-fluorophenyl)ethane-1,2-diyl) bis(azanylylidene))bis(methanylylidene))diphenol (**2a**). Yield 53%; Yellow solid; ^{1}H NMR (500 MHz, $CDCl_3$) δ 13.13 (s, 2H), 8.34 (s, 2H), 7.34–7.26 (m, 2H), 7.16 (ddd, J = 13.9, 8.1, 3.3 Hz, 6H), 6.96 (dd, J = 17.7, 8.8 Hz, 6H), 6.84 (t, J = 7.4 Hz, 2H), 4.69 (s, 2H).^{13}C NMR (126 MHz, $CDCl_3$) δ 166.41, 163.10, 161.14 , 160.82, 134.97, 132.82, 131.86, 129.37, 118.93, 118.43, 116.93, 115.49, 115.32, 79.54. ESI-MS: 457.2 ($[M+H]^+$).

[2,2'-((1E,1′E)-(((1R,2R)-1,2-bis(4-fluorophenyl)ethane-1,2-diyl) bis (azanylylidene))bis(methanylylidene))diphenol]gold(III) hexafluorophosphate (**2b**). Yield 13%; Red solid; ^{1}H NMR (500 MHz, CD_3CN) δ 7.98 (s, 2H), 7.79 (ddd, J = 8.6, 7.1, 1.6 Hz, 2H), 7.59 (dd, J = 8.0, 1.5 Hz, 2H), 7.43 (dd, J = 8.7, 5.2 Hz, 4H), 7.34 (d, J = 8.6 Hz, 2H), 7.24 (t, J = 8.8 Hz, 4H), 7.01 (t, J = 7.5 Hz, 2H), 5.74 (s, 2H).^{13}C NMR (126 MHz, CD_3CN) δ 164.77, 162.79, 160.86, 140.10, 136.48, 132.19 , 127.20, 119.89 , 119.02 , 118.13 , 116.93 , 116.75, 80.08. ESI-MS: 651.0 ($[M\text{-}PF_6]^+$).

meso-2,2'-((1E,1′E)-((1,2-bis(4-fluorophenyl)ethane-1,2-diyl) bis(azanylylidene))bis(methanylylidene))diphenol (**3a**). Yield 63%; Yellow solid; ^{1}H NMR (500 MHz, $CDCl_3$) δ 12.99 (s, 2H), 8.16 (s, 2H), 7.36–7.30 (m, 2H), 7.30–7.22 (m, 4H), 7.14 (dd, J = 7.6, 1.2 Hz, 2H), 7.06–6.94 (m, 6H), 6.87 (t, J = 7.4 Hz, 2H), 4.72 (s, 2H).^{13}C NMR (126 MHz, $CDCl_3$) δ 166.11, 163.20, 161.24, 160.75, 135.12, 132.86, 131.82, 129.53, 118.93, 118.47, 116.93, 115.61, 115.44, 79.27. ESI-MS: 457.2 ($[M+H]^+$).

meso-2,2'-((1E,1′E)-((1,2-bis(4-fluorophenyl)ethane-1,2-diyl) bis(azanylylidene))bis(methanylylidene))diphenol]gold(III) hexafluorophosphate (**3b**). Yield 17%; red solid; ^{1}H NMR (500 MHz, CD_3CN) δ 8.36 (s, 2H), 7.81 (t, J = 7.8 Hz, 2H), 7.61 (d, J = 8.0 Hz, 2H), 7.35 (d, J = 8.6 Hz, 2H), 7.20–7.14 (m, 4H), 7.09 (t, J = 8.7 Hz, 4H), 7.03 (t, J = 7.5 Hz, 2H), 5.81 (s, 2H). ^{13}C NMR (126 MHz, CD_3CN) δ 164.38, 162.51, 162.41, 161.01, 140.40, 136.42 , 131.78, 128.12, 119.99, 119.40, 118.22, 115.96, 115.78, 78.68. ESI-MS: 651.0 ($[M\text{-}PF_6]^+$).

d,l-2,2'-((1E,1′E)-((1,2-bis(4-fluorophenyl)ethane-1,2-diyl) bis(azanylylidene))bis(methanylylidene))diphenol (**4a**). Yield: 72%; yellow solid; ^{1}H NMR (DMSO-d_6): δ 13.15 (s, 2H), 8.56 (s, 2H), 7.27–7.38 (m, 8H), 7.07–7.15 (t, 3 J = 8.81 Hz, 4H); 6.81–6.89 (m, 4H); 5.11 (s, 2H). ESI-MS: 457.4 ($[M+H]^+$).

d,l-2,2'-((1E,1′E)-((1,2-bis(4-fluorophenyl)ethane-1,2-diyl) bis(azanylylidene))bis(methanylylidene))diphenol]gold(III) hexafluorophosphate (**4b**). Yield 56%; Red solid;^{1}H NMR (DMSO-d_6): δ 8.19 (s, 2H), 7.74–7.82 (m, 4H), 7.46–7.51 (m, 4H), 7.27–7.34 (m, 6H), 6.94–6.98 (m, 2H), 5.90 (s, 2H). ESI-MS: 651.1 ($[M\text{-}PF_6]^+$).

4.2.3. X-ray crystallographic analysis

Monocrystal of **4b** was obtained by slowly diffusing methanol into concentrated solution of **4b** of dichloromethane. The data was collected at 193 K on a BRUKER Smart APEX II CCD area-detector diffractometer with graphite-monochromated Mo Kα radiation (λ = 0.71073 Å). Single crystal structure analysis and correction were performed using the SHELX-2014 kit program. More detail data about complex **4b** seen in supporting information via www.ccdc.cam.ac.uk/structures at a CCDC number: 1975710 or at a DOI number: 10.5517/ccdc.csd.cc249wly.

4.2.4. Stereostructure analysis

Complexes **1a, 2a, 1b, 2b** and ingredients were dissolved in THF (100 μM). CD spectra were recorded in a cuvette of 1 cm path length, over the range of 200–800 nm, the scan rate of 200 nm min^{-1} and the slit width of 3000 μm.

4.2.5. Stability analysis

1b was mixed with 10% D_2O+90% DMSO-d_6 over a period of 168 h and ^{1}H NMR spectra were taken in different times.

4.2.6. Interaction with GSH and NAC

The solution with 50% DMSO-d_6 + 50% D_2O containing the complex **1b** (0.25 mM) and GSH (0.25 mM) or NAC (0.25 mM) was analysed by UV-Vis and ^{1}H NMR at different times.

4.2.7. DNA binding test

The interaction of complex **1b** with CT-DNA was studied by UV–Vis and CD spectra in PBS buffer (10 mM, pH = 7.2). The CT-DNA (1.24 mM) stock solution was stored in a refrigerator at 4 °C and stored for less than 5 days before use.

4.2.8. UV–Vis spectral analysis

The stock solution of complex **1b** was diluted 200 times with PBS buffer to obtain 1.0 × 10^{-5} M solution (3 mL). Then CT-DNA stock solution was added gradually. When the mixture solution had reacted sufficiently, the UV–Vis absorption spectra were recorded.

4.2.9. CD spectral analysis

Complex **1b** was dissolved in PBS buffer (10 mM, pH = 7.2). A series of samples containing CT-DNA (50 μM) and increasing concentrations of complex **1b** (r_b = [complex]/[DNA]), r_b = 0.0, 0.02, 0.05, 0.1) were prepared and incubated for 24 h at 37 °C. CD spectra was recorded in a cuvette of 1 cm path length, over the range of 200–500 nm, the scan rate of 200 nm min^{-1} and the slit width of 3000 μm.

4.3. Growth inhibitory assay

Cells were seeded into 96-well plates at a density of 2 × 10^3 per well and allowed to attach overnight in DMEM containing 10% heat-inactivated FBS. **1b** dissolved in DMSO and the control group was treated with 0.1% DMSO. The antiproliferation effect of compounds was measured using the MTT cytotoxicity assay. The specific steps are as follows: adding 5% MTT (5 mg/mL, PBS) reagent to the cells treated with the compounds, incubating for 4 h at 37 °C, adding 200 μL DMSO and shaking 10 min. Detected the absorbance at 490 nm. The concentration range of each complex was selected based on the cytotoxicity. The growth inhibitory rates of the complexes were calculated as $(OD_{control} - OD_{test})/OD_{control} \times 100\%$. Half maximal inhibitory concentration (IC_{50}) value of the drug concentration corresponding to the inhibition rate at 50% was calculated using Graphpad Prism 5 statistical analysis. All experiments were conducted three times to ensure the reproducibility of the results.

4.4. Purified TrxR enzyme assay

DMSO or with **1b** (0.125 μM, 0.25 μM, 0.5 μM, 1 μM, 2 μM) and rat liver TrxR (0.15 U) were dissolved in 50 μL reaction buffer. Added 225 μL of reaction mixture to each well. And the reaction was started by adding 25 μL solution of 20 mM DTNB. After appropriate mixing, record the absorption data at 405 nm with a microplate reader. The increase in TNB concentration over time follows a linear trend ($r^2 \geq 0.99$), and the enzyme activity is calculated as its slope (increased absorbance per 30 s). For each test compound, it was confirmed by non-interference test components by using a negative control experiment without an enzyme solution.

4.5. PCR assay

Trizol reagent was used to extract HepG2 RNA according to the manufacturer's instructions. Real-time PCR was executed by 7500 RT-PCR system as described previously [51,52]. The mRNA levels of the target genes were calculated and results are from triplicate experiments. The following primers (GenScript, Nanjing, China) were used: β-actin: (forward) 5′-TGTGGATCAGCAAGCAGGAGTA-3′,

(reverse) 5′-TGCGCAAGTTAGGTTTT GTCA-3′.

TrxR: (forward) 5′-GCCCTGCAAGACTCTCGAAATTA-3′,

(reverse) 5′-GCCCATAAGCATTCTCATAGACGA-3′.

4.6. Cellular activities of TrxR assay

HepG2 cells were treated with different concentrations of **1b** for 24 h. Then, the culture was carefully discarded and washed twice with PBS. Total cell protein was extracted by treatment with RIPA buffer (150 mM NaCl, 50 mM Tris-HCl, pH 7.5, 0.5% deoxycholate, 2 mM EDTA, 0.1% SDS, 1% Triton X-100, 1 mM PMSF and 1 mM Na_3VO_4) in an ice bath and quantified using the Bradford program. The activity of TrxR in cells was determined according to the TrxR activity detection kit (Beijing Solarbio Science & Technology).

4.7. Immunofluorescence staining

HepG2 cells were seeded in 24-well plates and cultured for 24 h, then treated with **1b** for another 24 h. Incubating with antibodies overnight at 4 °C, followed by treating with anti-rabbit IgG for 2 h and then the cells were washed for three times. The nuclei of HepG2 cancer cells were dyed by 4′,6-Diamidino-2-phenylindole (DAPI). Immunofluorescence was detected with a fluorescence microscope (Leica DMi8).

4.8. Western blot analysis

HepG2 cells (1×10^6 cells/well) were inoculated into a 10 cm diameter tissue culture dish (10 mL/well), and then treated with **1b** at different dose for another 24 h. Cell lysates were prepared using protease and phosphatase inhibitors. BCA assay kits were used to determine protein levels. After the separation process, the proteins were imprinted onto the PVDF membranes and blocked overnight, and incubated with the suitable secondary antibody for 2 h, then washed with PBST, the bands of protein detected by chemiluminescence procedure (ECL, Amersham).

4.9. Intracellular ROS measurement and ROS-ERS colocalization

HepG2 cells (2×10^4 cells/well) were inoculated in 24-well plates and treated with **1b** incubated for 24 h, then washed with PBS and 10 μM CM-DCFH2-DA for 20 min at 37 °C in darkness. ROS generation in HepG2 cells was assessed by the fluorescent probe CM-DCFH2-DA (Molecular Probes, Invitrogen). The ER-Tracker Red was used to examine the effects of binding to sulfonylurea receptors in the ER. The fluorescence increase was visualized by a Leica DMi8 fluorescent microscopy.

4.10. Measurement of MMP

HepG2 cells (2×10^4 cells/mL) were seeded on cover slips in a 24-well plate and incubated for 24 h in supplemental medium and then treated with **1b** or DMSO for 2 h. After that, the cells were treated with JC-1 (5 μM) for 30 min, washed with PBS buffer for three times, the cell staining was observed with a fluorescence microscope.

4.11. Cell cycle arrest and apoptosis analysis

HepG2 cells (2×10^4 cells/well) were seeded in 6-well plates and cultured for 24 h followed by the treatment with DMSO or **1b** for another 72 h. Cellular DNA flow cytometric kits (Nanjing Key Gen Biotech) were used according to the manufacturer's protocol to determine the stage of the cell cycle, specifically G0/G1, S, or G2/M, by flow cytometry (BD, Franklin Lakes, NJ, USA). Apoptosis was determined by FITC-labeled annexin V/PI double staining. The percentages of annexin-positive HepG2 cells without PI staining were determined by flow cytometry (FACS Calibur; BD). The data were analysed using cell quest software.

4.12. Assessment of LDH release

HepG2 cells were cultured in 96-well plates with the corresponding treatment. LDH release was determined using commercially available kits according to the manufacturer's instructions (Jiancheng, China). Absorbance was measured at a wavelength of 450 nm. The data were expressed as a percentage of the control values. Each culture was performed in three duplicates.

4.13. Chronic liver cancer model caused by CCl_4

All experiments involving mice were approved by the institutional and local ethics committee (Beijing Weitong Lihua Laboratory Animal Technology Co., Ltd., China). According to National Institutes of Health guidelines, all mice were gained humane sympathy. Four-week-old male ICR mice (18−22 g) were randomly divided into 3 groups of 6 mice each, and all animals were fed under standardized conditions with a light/dark cycle of appropriate humidity at room temperature, and provided water and standard pathogen-free feed. Group one was the vehicle control, in which the mice were treated without CCl_4 or **1b** treatment. Group two was the CCl_4 model group. Group three was the drug treatment group, in which the mice received CCl_4 and **1b** at the same time. Groups two and three were injected with CCl_4 (5 mL/kg) three times a week and treated for 16 weeks to induce liver injury. Groups three was intraperitoneally injected with **1b** (20 mg/kg) daily for the last two weeks. After 16 weeks, collected the liver and blood and the livers were fixed in 4% paraformaldehyde buffer for subsequent Western blot analysis and histological analysis.

Declaration of competing interest

The authors declare no competing financial interests.

Acknowledgments

We thank the financial supports of the National Natural Science Foundation of China (No.81703337), the Priority Academic Program Development of Jiangsu Higher Education Institutions (Integration of Chinese and Western Medicine), the Jiangsu Specially-Appointed Professors program, the Open Project of State Key Laboratory of Natural Medicines (No. SKLNMKF201808, SKLNMKF201712), the State Key Laboratory of Coordination Chemistry, Nanjing University and the Six Talent Peaks Project in Jiangsu Province of China (No. SWYY-069).

Appendix A. Supplementary data

Supplementary data to this article can be found online at https://doi.org/10.1016/j.ejmech.2020.112234.

References

[1] R.M. Feng, Y.N. Zong, S.M. Cao, R.H. Xu, Current cancer situation in China: good or bad news from the 2018 global cancer statistics? Canc. Commun. 39 (2019) 22.

[2] Y. Jiang, A. Sun, Y. Zhao, W. Ying, H. Sun, X. Yang, B. Xing, W. Sun, L. Ren, B. Hu, C. Li, L. Zhang, G. Qin, M. Zhang, N. Chen, M. Zhang, Y. Huang, J. Zhou, Y. Zhao,

M. Liu, X. Zhu, Y. Qiu, Y. Sun, C. Huang, M. Yan, M. Wang, W. Liu, F. Tian, H. Xu, J. Zhou, Z. Wu, T. Shi, W. Zhu, J. Qin, L. Xie, J. Fan, X. Qian, F. He, C. Chinese, Human Proteome Project, Proteomics identifies new therapeutic targets of early-stage hepatocellular carcinoma, Nature 567 (2019) 257–261.
[3] R. Siegel, D. Naishadham, A. Jemal, Cancer statistics, 2013, CA A Cancer J. Clin. 63 (2013) 11–30.
[4] P. Newell, A. Villanueva, S.L. Friedman, K. Koike, J.M. Llovet, Experimental models of hepatocellular carcinoma, J. Hepatol. 48 (2008) 858–879.
[5] D. Lee, I.M. Xu, D.K. Chiu, J. Leibold, A.P. Tse, M.H. Bao, V.W. Yuen, C.Y. Chan, R.K. Lai, D.W. Chin, D.F. Chan, T.T. Cheung, S.H. Chok, C.M. Wong, S.W. Lowe, I.O. Ng, C.C. Wong, Induction of oxidative stress through inhibition of thioredoxin reductase 1 is an effective therapeutic approach for hepatocellular carcinoma, Hepatology 69 (2019) 1768–1786.
[6] S.E. Eriksson, S. Prast-Nielsen, E. Flaberg, L. Szekely, E.S. Arner, High levels of thioredoxin reductase 1 modulate drug-specific cytotoxic efficacy, Free Radic. Biol. Med. 47 (2009) 1661–1671.
[7] J. Zhang, X. Li, X. Han, R. Liu, J. Fang, Targeting the thioredoxin system for cancer therapy, Trends Pharmacol. Sci. 38 (2017) 794–808.
[8] O. Rackham, A.M. Shearwood, R. Thyer, E. McNamara, S.M. Davies, B.A. Callus, A. Miranda-Vizuete, S.J. Berners-Price, Q. Cheng, E.S. Arner, A. Filipovska, Substrate and inhibitor specificities differ between human cytosolic and mitochondrial thioredoxin reductases: implications for development of specific inhibitors, Free Radic. Biol. Med. 50 (2011) 689–699.
[9] C. Li, Y. Peng, B. Mao, K. Qian, Thioredoxin reductase: a novel, independent prognostic marker in patients with hepatocellular carcinoma, Oncotarget 6 (2015) 17792–17804.
[10] B. Fu, W. Meng, X. Zeng, H. Zhao, W. Liu, T. Zhang, TXNRD1 is an unfavorable prognostic factor for patients with hepatocellular carcinoma, BioMed. Res. Int. 2017 (2017), 4698167.
[11] T. Zou, C.T. Lum, C.N. Lok, J.J. Zhang, C.M. Che, Chemical biology of anticancer gold(III) and gold(I) complexes, Chem. Soc. Rev. 44 (2015) 8786–8801.
[12] D. Benitez, N.D. Shapiro, E. Tkatchouk, Y. Wang, W.A. Goddard 3rd, F.D. Toste, A bonding model for gold(I) carbene complexes, Nat. Chem. 1 (2009) 482–486.
[13] L. Boselli, I. Ader, M. Carraz, C. Hemmert, O. Cuvillier, H. Gornitzka, Synthesis, structures, and selective toxicity to cancer cells of gold(I) complexes involving N-heterocyclic carbene ligands, Eur. J. Med. Chem. 85 (2014) 87–94.
[14] E. Hatem, S. Azzi, N. El Banna, T. He, A. Heneman-Masurel, L. Vernis, D. Baille, V. Masson, F. Dingli, D. Loew, B. Azzarone, P. Eid, G. Baldacci, M.E. Huang, Auranofin/Vitamin C: a novel drug combination targeting triple-negative breast cancer, J. Natl. Cancer Inst. 111 (2018) 597–608.
[15] B. Liang, W. Shao, C. Zhu, G. Wen, X. Yue, R. Wang, J. Quan, J. Du, X. Bu, Mitochondria-targeted approach: remarkably enhanced cellular bioactivities of TPP2a as selective inhibitor and probe toward TrxR, ACS Chem. Biol. 11 (2016) 425–434.
[16] I. Ott, X. Qian, Y. Xu, D.H. Vlecken, I.J. Marques, D. Kubutat, J. Will, W.S. Sheldrick, P. Jesse, A. Prokop, C.P. Bagowski, A gold(I) phosphine complex containing a naphthalimide ligand functions as a TrxR inhibiting antiproliferative agent and angiogenesis inhibitor, J. Med. Chem. 52 (2009) 763–770.
[17] G.X. Hou, P.P. Liu, S. Zhang, M. Yang, J. Liao, J. Yang, Y. Hu, W.Q. Jiang, S. Wen, P. Huang, Elimination of stem-like cancer cell side-population by auranofin through modulation of ROS and glycolysis, Cell Death Dis. 9 (2018) 89.
[18] B. Bertrand, A. Casini, A golden future in medicinal inorganic chemistry: the promise of anticancer gold organometallic compounds, Dalton Trans. 43 (2014) 4209–4219.
[19] S. Nobili, E. Mini, I. Landini, C. Gabbiani, A. Casini, L. Messori, Gold compounds as anticancer agents: chemistry, cellular pharmacology, and preclinical studies, Med. Res. Rev. 30 (2010) 550–580.
[20] I. Ott, On the medicinal chemistry of gold complexes as anticancer drugs, Coord. Chem. Rev. 253 (2009) 1670–1681.
[21] T. Zou, C.T. Lum, C.-N. Lok, W.-P. To, K.-H. Low, C.-M. Che, A binuclear gold(I) complex with mixed bridging diphosphine and bis(N-heterocyclic carbene) ligands shows favorable thiol reactivity and inhibits tumor growth and angiogenesis in vivo, Angew. Chem. Int. Ed. 53 (2014) 5810–5814.
[22] O. Karaca, V. Scalcon, S.M. Meier-Menches, R. Bonsignore, J. Brouwer, F. Tonolo, A. Folda, M.P. Rigobello, F.E. Kuhn, A. Casini, Characterization of hydrophilic gold(I) N-heterocyclic carbene (NHC) complexes as potent TrxR inhibitors using biochemical and mass spectrometric approaches, Inorg. Chem. 56 (2017) 14237–14250.
[23] C. Schmidt, B. Karge, R. Misgeld, A. Prokop, M. Bronstrup, I. Ott, Biscarbene gold(i) complexes: structure-activity-relationships regarding antibacterial effects, cytotoxicity, TrxR inhibition and cellular bioavailability, Medchemcomm 8 (2017) 1681–1689.
[24] A. Casini, R.W. Sun, I. Ott, Medicinal chemistry of gold anticancer metallodrugs, Met. Ions. Life Sci. 18 (2018) 221–231.
[25] S.J. Berners-Price, A. Filipovska, Gold compounds as therapeutic agents for human diseases, Metallomics 3 (2011) 863–873.
[26] T. Zou, C.T. Lum, S.S. Chui, C.M. Che, Gold(III) complexes containing N-heterocyclic carbene ligands: thiol “switch-on” fluorescent probes and anticancer agents, Angew. Chem. Int. Ed. 52 (2013) 2930–2933.
[27] S.K. Fung, T. Zou, B. Cao, P.Y. Lee, Y.M. Fung, D. Hu, C.N. Lok, C.M. Che, Cyclometalated gold(III) complexes containing N-heterocyclic carbene ligands engage multiple anti-cancer molecular targets, Angew. Chem. Int. Ed. 56 (2017) 3892–3896.
[28] M. Proetto, W. Liu, A. Hagenbach, U. Abram, R. Gust, Synthesis, characterization and in vitro antitumour activity of a series of novel platinum(II) complexes bearing Schiff base ligands, Eur. J. Med. Chem. 53 (2012) 168–175.
[29] R. Gust, I. Ott, D. Posselt, K. Sommer, Development of cobalt(3,4-diarylsalen) complexes as tumor therapeutics, J. Med. Chem. 47 (2004) 5837–5846.
[30] H. Kim, Y. Nguyen, C.P. Yen, L. Chagal, A.J. Lough, B.M. Kim, J. Chin, Stereospecific synthesis of C2 symmetric diamines from the mother diamine by resonance-assisted hydrogen-bond directed diaza-cope rearrangement, J. Am. Chem. Soc. 130 (2008) 12184–12191.
[31] J.J. Yan, R.W. Sun, P. Wu, M.C. Lin, A.S. Chan, C.M. Che, Encapsulation of dual cytotoxic and anti-angiogenic gold(III) complexes by gelatin-acacia microcapsules: in vitro and in vivo studies, Dalton Trans. 39 (2010) 7700–7705.
[32] M. Bian, Y. Sun, Y. Liu, Z. Xu, R. Fan, Z. Liu, W. Liu, A gold(I) complex containing an oleanolic acid derivative as a potential anti-ovarian cancer agent via inhibiting TrxR and activating ROS-mediated ERS, Chem. Eur J. (2020), https://doi.org/10.1002/chem.202000045.
[33] J. Zhang, B. Zhang, X. Li, X. Han, R. Liu, J. Fang, Small molecule inhibitors of mammalian thioredoxin reductase as potential anticancer agents: an update, Med. Res. Rev. 39 (1) (2018) 5–39.
[34] S. Gromer, L.D. Arscott, C.H. Williams Jr., R.H. Schirmer, K. Becker, Human placenta thioredoxin reductase. Isolation of the selenoenzyme, steady state kinetics, and inhibition by therapeutic gold compounds, J. Biol. Chem. 273 (1998) 20096–20101.
[35] K.B. Huang, F.Y. Wang, X.M. Tang, H.W. Feng, Z.F. Chen, Y.C. Liu, Y.N. Liu, H. Liang, Organometallic gold(III) complexes similar to tetrahydroisoquinoline Induce ER-stress-mediated apoptosis and pro-death autophagy in A549 cancer cells, J. Med. Chem. 61 (2018) 3478–3490.
[36] V.C. Keil, F. Funke, A. Zeug, D. Schild, M. Muller, Ratiometric high-resolution imaging of JC-1 fluorescence reveals the subcellular heterogeneity of astrocytic mitochondria, Pflügers Archiv 462 (2011) 693–708.
[37] E. Hocsak, V. Szabo, N. Kalman, C. Antus, A. Cseh, K. Sumegi, K. Eros, Z. Hegedus, F. Gallyas Jr., B. Sumegi, B. Racz, PARP inhibition protects mitochondria and reduces ROS production via PARP-1-ATF4-MKP-1-MAPK retrograde pathway, Free Radic. Biol. Med. 108 (2017) 770–784.
[38] J.J. Zhang, R.W.Y. Sun, C.M. Che, A dual cytotoxic and anti-angiogenic water-soluble gold(III) complex induces endoplasmic reticulum damage in HeLa cells, Chem. Commun. 48 (2012) 3388.
[39] M. Bian, R. Fan, S. Zhao, W. Liu, Targeting the thioredoxin system as a strategy for cancer therapy, J. Med. Chem. 62 (2019) 7309–7321.
[40] C.G. Hartinger, P.J. Dyson, Bioorganometallic chemistry–from teaching paradigms to medicinal applications, Chem. Soc. Rev. 38 (2009) 391–401.
[41] W.H. Ang, M. Myint, S.J. Lippard, Transcription inhibition by platinum-DNA cross-links in live mammalian cells, J. Am. Chem. Soc. 132 (2010) 7429–7435.
[42] G. Gasser, I. Ott, N. Metzler-Nolte, Organometallic anticancer compounds, J. Med. Chem. 54 (2011) 3–25.
[43] M. Raoof, S.J. Corr, C. Zhu, B.T. Cisneros, W.D. Kaluarachchi, S. Phounsavath, L.J. Wilson, S.A. Curley, Gold nanoparticles and radiofrequency in experimental models for hepatocellular carcinoma, Nanomedicine 10 (2014) 1121–1130.
[44] S. Mancarella, S. Krol, A. Crovace, S. Leporatti, F. Dituri, M. Frusciante, G. Giannelli, Validation of hepatocellular carcinoma experimental models for TGF-beta promoting tumor progression, Cancers 11 (2019) 112–119.
[45] R. Fan, M. Bian, L. Hu, W. Liu, A new rhodium(I) NHC complex inhibits TrxR: in vitro cytotoxicity and in vivo hepatocellular carcinoma suppression, Eur. J. Med. Chem. 183 (2019), 111721.
[46] X. Zheng, W. Ma, R. Sun, H. Yin, F. Lin, Y. Liu, W. Xu, H. Zeng, Butaselen prevents hepatocarcinogenesis and progression through inhibiting thioredoxin reductase activity, Redox Biol. 14 (2018) 237–249.
[47] T. Uehara, I.P. Pogribny, I. Rusyn, The DEN and CCl4 -induced mouse model of fibrosis and inflammation-associated hepatocellular carcinoma, Curr. Protoc. Pharmacol. 66 (2014) 14301–14310.
[48] K. Reyes-Gordillo, R. Shah, J. Arellanes-Robledo, Y. Cheng, J. Ibrahim, P.L. Tuma, Akt1 and Akt2 isoforms play distinct roles in regulating the development of inflammation and fibrosis associated with alcoholic liver disease, Cells 8 (2019) 21–32.
[49] M. Pawlak, P. Lefebvre, B. Staels, Molecular mechanism of PPARalpha action and its impact on lipid metabolism, inflammation and fibrosis in non-alcoholic fatty liver disease, J. Hepatol. 62 (2015) 720–733.
[50] J.M. Heilman, T.J. Burke, C.J. McClain, W.H. Watson, Transactivation of gene expression by NF-kappaB is dependent on thioredoxin reductase activity, Free Radic. Biol. Med. 51 (2011) 1533–1542.
[51] M. Bian, X. Chen, C. Zhang, H. Jin, F. Wang, J. Shao, A. Chen, F. Zhang, S. Zheng, Magnesium isoglycyrrhizinate promotes the activated hepatic stellate cells apoptosis via endoplasmic reticulum stress and ameliorates fibrogenesis in vitro and in vivo, Biofactors 43 (2017) 836–846.
[52] M. Bian, J. He, H. Jin, N. Lian, J. Shao, Q. Guo, S. Wang, F. Zhang, S. Zheng, Oroxylin A induces apoptosis of activated hepatic stellate cells through endoplasmic reticulum stress, Apoptosis 24 (2019) 905–920.